Journal of The Electrochemical Society

OPEN ACCESS

Electrodeposition onto Conductive Additive-Impregnated 3D Printed Polylactic Acid Electrodes

To cite this article: Sally O'Hanlon and Colm O'Dwyer 2022 *J. Electrochem. Soc.* **169** 082514

Journal of The Electrochemical Society, 2022 **169** 082514

Electrodeposition onto Conductive Additive-Impregnated 3D Printed Polylactic Acid Electrodes

Sally O'Hanlon[1] **and Colm O'Dwyer**[1,2,3,z]

[1]*School of Chemistry, University College Cork, Cork, T12 YN60, Ireland*
[2]*AMBER@CRANN, Trinity College Dublin, Dublin 2, Ireland*
[3]*Environmental Research Institute, University College Cork, Cork T23 XE10, Ireland*

Conductive additive-impregnated polylactic acid can be coated with vanadium oxide (V_2O_5) by electrodeposition. By thermal pre-treatment of the thermoset printed electrode structure comprising a graphite-PLA composite, the conductivity of the composite material is improved by exposing the graphite at the outer surface by surface segregation, that is ordinarily buried within the plastic. This promotes quite effective electrodeposition under potentiostatic conditions, allowing conformal coating a complex electrode surface and structure with V_2O_5. The surface coating and electrode were analysed using Raman scattering spectroscopy, X-ray diffraction, energy dispersive X-ray analysis and scanning electron microscopy, and details the relationship between electrodeposition parameters and the quality of the deposit on the PLA electrode.
 [DOI: 10.1149/1945-7111/ac87d8]

Manuscript submitted April 12, 2022; revised manuscript received August 5, 2022. Published August 18, 2022. *This paper is part of the JES Focus Issue on Nucleation and Growth: Measurements, Processes, and Materials.*

3D printing is fast becoming a manufacturing protocol for prototyping many technologies and materials including those in electrochemical science and technology such as energy storage and conversion and materials deposition.[1,2] 3D printing has become a simple method for prototyping composite electrodes for electrochemistry,[3,4] and it is clear that some work remains to improve or modify the nature of the material-processing-electrochemistry interface that is critical to each 3D printed electrode.[5–7]

3D printing and additive manufacturing (AM) in general, also provides an opportunity to form complex structures with ease compared to equally complex synthetic protocols and material assembly requirements.[8] And printing can in principle extend to metals, plastics, conducting composites, inorganic materials and fillers, polymeric ionically conducting electrolytes, and even bioinspired hierarchically structured composites.[9]

Additive manufacturing methods[10–13] have played some role in enabling flexible, stretchable[14] and ultra-thin batteries. Recently, energy storage options have been included as structural devices, forming panels on vehicles.[15] Since anode and cathode materials were first 3D printed to make microbatteries[16–18] and composite batteries,[19] other groups have endeavoured to realise the 3D printable Li-ion battery using a fused filament fabrication (FFF) or fused deposition modelling (FDM). The search for an optimized route to 3D print all components of a battery, either separately or sequentially (anode, separator, cathode and outer casing) is underway.[20] Incorporating electrolytes is more difficult still, particularly organic-based chemistries that are incompatible with most plastics, but progress has been made for polymer electrolytes via 3D printing.[21,22] Reyes et al.[23] and Maurel et al.[24] have made recent advances in controlling the additives and conductivity of PLA, making a 3D printed cell and enhanced conductivity PLA anode, respectively. Low electronic conductivity was one reason for modifying the graphitic content of PLA, identified by Foster et al.[25] Reyes et al. also realised the limited ionic conductivity of PLA,[26,27] even when electrical conductivity was enhanced, needed to be improved. Maurel et al.[24] also experimented with ways to make their own conductive PLA composites for extrusion and printing, successfully showing a PLA with high volume fraction of graphite is possible.

Rheologically, high volume fractions of conductive additives, electrolyte incorporation and active materials as fillers, all affect the brittleness and consistency of polylactic acid (PLA) or related plastics during filament extrusion at elevated temperature[18] with further influence on the electrochemical response of the material in a battery cell. PLA that covers the outer surface of any electrode material limits its electrochemical activity with electrolyte (PLA insulates the graphene-active material electrical interface in such composites), adding dead weight and limiting the capacity, electrochemical activity or the ability to be conformally coated with an electrodeposited material.

Since mass loading in energy storage and film coverage for a range of other reasons and technologies is important for 3D printable devices,[8,28–35] we surveyed various approaches to coating of 3D printable thermoset plastics. The underpinning demand is for electrically conductive thermosetting composites of other materials and methods[36–39] that avoid mechanical limitations of brittleness with high graphite of carbon loading. Coating onto plastic electrode surfaces is not a typical approach, but the additive manufacturing capabilities nowadays provide ways to make complex structures but also mixture of materials that are printable. While the latter capability is still being developed, the interim approach is direct deposition onto printed electrodes. One benefit of electrodeposition is the conformal coating and formal electrical interfacing with the underlying substrate or current collector. An obvious disadvantage is the dependence on good or at least uniform conductivity at the surface of the substrate, to ensure uniform coating.

Here, we show that vanadium oxide can be directly electrodeposited on 3D printed structures composed of thermoset filaments of polylactic acid that was impregnated with graphitic conductive additives. Using a paddle-shaped design of an electrode, we show how thermal pre-treatment modifies that PLA surface to relieve the graphite and ensure a reasonably good electrical conductivity to allow electrodeposition on a surface made of plastic.

Experimental

3D printing of conductive PLA electrodes.—The PLA electrodes were designed using 3D computer aided design (CAD) software and printed using a MakerBot Replicator 2X. Paddle-structured electrodes were 18 mm long, 2 mm thick (2 layers of printed filament) and had a circular electrode regions of 12 mm in diameter. The conductive polylactic acid (c-PLA) purchased from Proto-pasta. After printing, the c-PLA electrodes were heated to 300 °C for 24 h. After heating above the PLA melting point, we note that the printed graphite-PLA structure does not collapse.

[z]E-mail: c.odwyer@ucc.ie

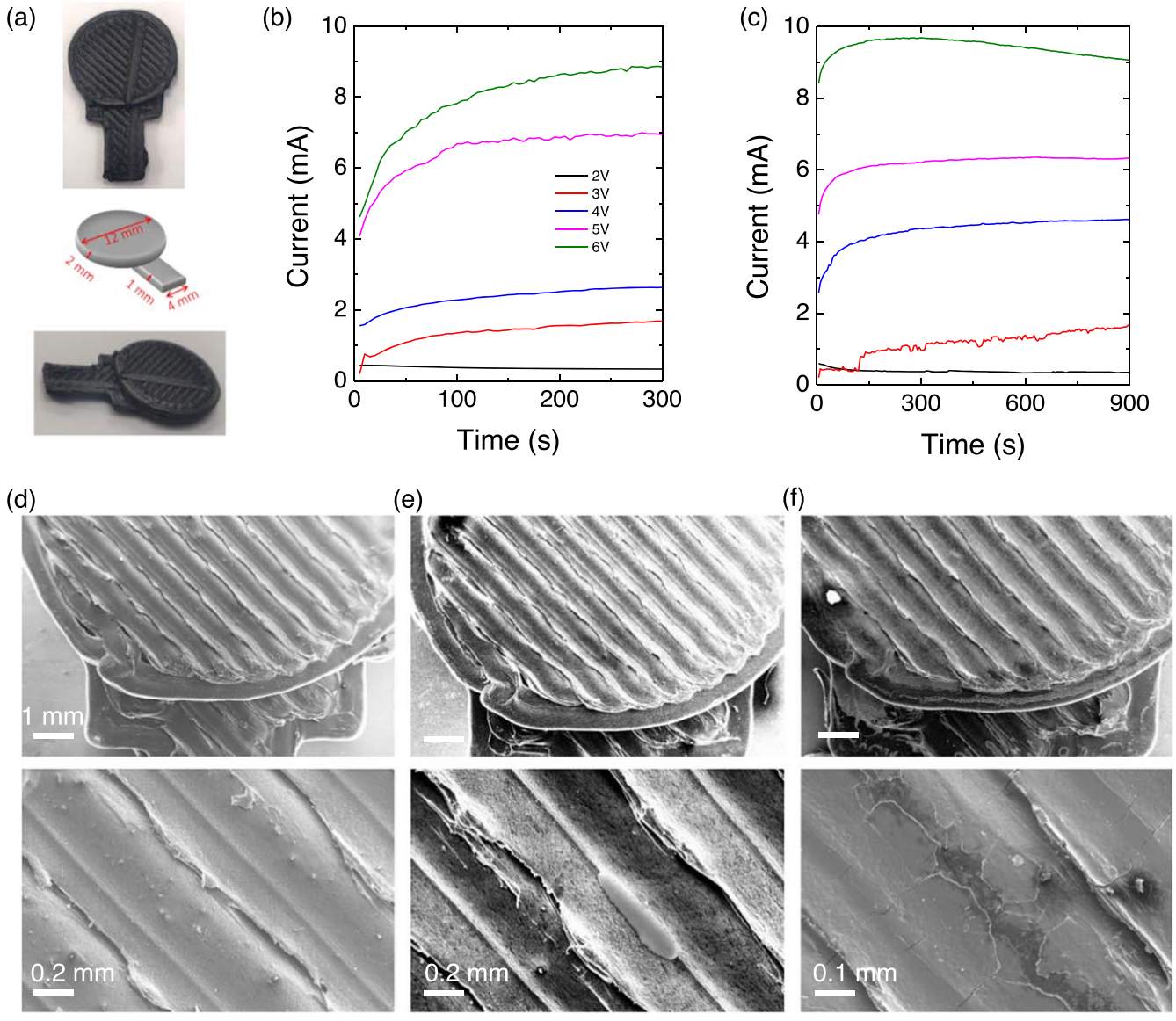

Figure 1. (a) Images and schematic model of 3D printed electrodes using conductive additive-impregnated PLA. (b) Potentiostatic transients of these 3D printed c-PLA electrodes in vanadyl sulfate electrolytes for V_2O_5 electrodeposition over 300 s and (c) 900 s duration using annealed 3D printed electrodes. Transients were recorded from 2–6 V (vs SCE) at room temperature. (d) SEM image of the electrode as-printed. (e) SEM image of the non-heated electrode showing very limited V_2O_5 formation and (f), good coverage of the 3D printed electrode after heating that exposes surface graphite.

Imaging and spectroscopic analysis.—Surface morphology of the samples was examined by scanning electron microscopy (SEM) performed on an FEI Quanta 650 FEG high resolution SEM with operating voltages of 10–20 kV equipped with an Oxford Instruments X-MAX 20 large area Si diffused EDX detector. EDX analysis included line scan spectra and areal mapping of specific elements (V, C, O and S). Raman scattering was acquired using a QE65 PRO Ocean Optics spectrometer with a 50 μm slit width. Excitation was provided by a Laser Quantum GEM DPSS single transverse mode CW green laser emitting at $\lambda = 532$ nm. The spectral resolution of the spectrometer ranges from 17.5–10.5 cm^{-1} between 300–4000 cm^{-1}. The laser source was focused onto the sample surface through an objective of 4×, 10×, 20× or 40× magnifications with numerical apertures (N.A.) of 0.10, 0.25, 0.40 and 0.60, respectively. Spectra were collected under a variety of different laser powers from 10 mW to 100 mW. The laser power densities (LPDs) calculated from these settings range between 15.41 W cm^{-1} for 4× magnification with 10% laser power to 924.3 W cm^{-1} for 40× magnification with 100% laser power, and care was taken to avoid localized heating that affected phonon modes in the spectra. Spectra were calibrated against the main optical phonon of (100)-oriented single crystal Si wafer pieces at 520 cm^{-1}.

Electrodeposition of V_2O_5.—Vanadium pentoxide was grown by electrodeposition at room temperature using a VersaSTAT3 Potentiostat. Potentials between 1 V and 6 V was applied for either 300s or 900s at each voltage vs a saturated calomel (SCE) reference electrode in a three-electrode cell with a platinum mesh as counter electrode. The electrolyte was made by adding 2.53 g of $VOSO_4.\chi H_2O$, used as purchased from Sigma Aldrich, to a 1:1 (v/v) mixture of 20 ml of deionized water and 20 ml of ethanol to form a 0.25 mol dm^{-3} $VOSO_4.\chi H_2O$ solution.

Materials characterization and analysis.—XRD analysis was performed using a Phillips X'pert PW3719 diffractometer using Cu Kα radiation. (Cu Kα, $\lambda = 0.15418$ nm, operation voltage 40 kV, current 40 mA). XPS spectra were acquired on an Oxford Applied Research Escabase XPS system equipped with a CLASS VM 100 mm mean radius hemispherical electron energy analyzer with

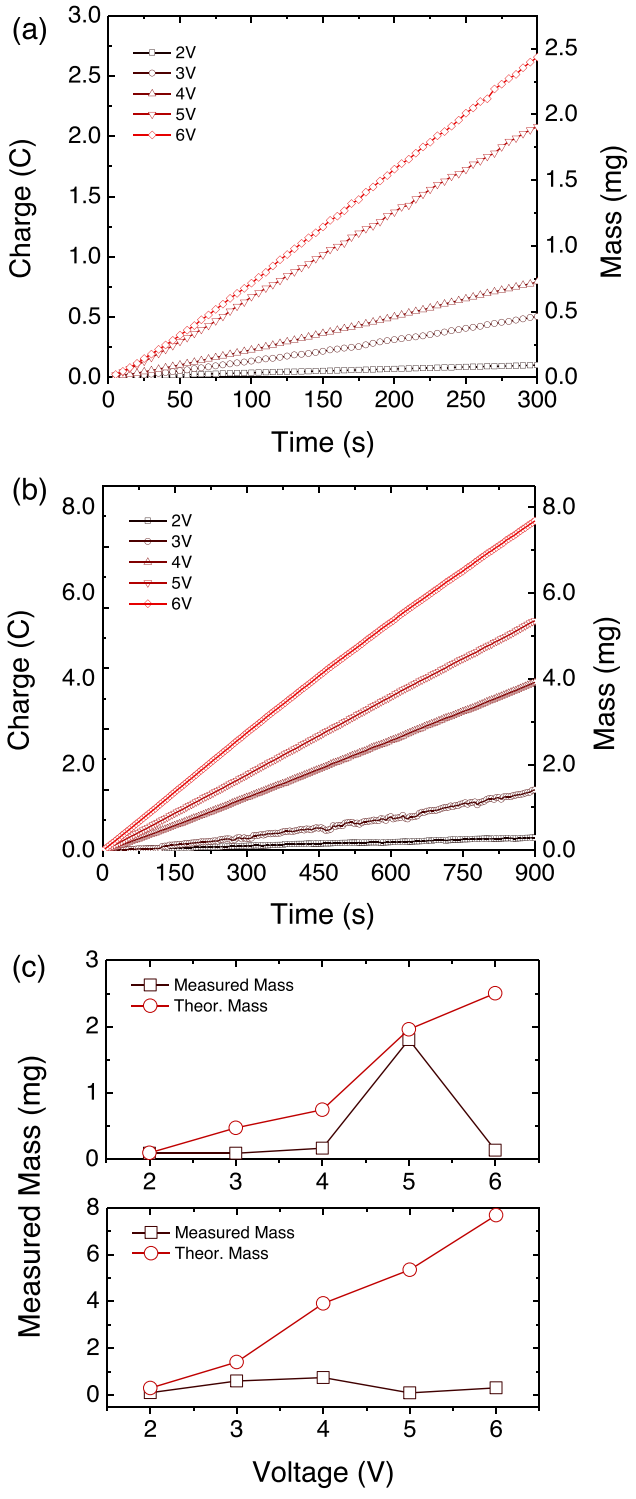

Figure 2. Cumulative charge passed during electrodeposition of V_2O_5 onto 3D printed c-PLA electrodes by integration of the potentiostatic I(t) curves from 2.0–6.0 V over (a) 300 s and (b) 900 s. The theoretical mass at full Faradaic efficiency is also shown in the right axis. (c) Ratio of the theoretical mass to measured mass for all electrodeposits from 2.0–6.0 V after 300 s (top) and 900 s (bottom).

multichannel detectors in an analysis chamber with a base pressure of 5.0×10^{-10} mbar. Survey scans were recorded between 0 and 1400 eV with a step size of 0.7 eV, dwell time of 0.5s, and pass energy of 100 eV. Core level scans were acquired with a step size of 0.1 eV, dwell time of 0.5 s, and pass energy of 20 eV averaged over 10 scans. A non-monochromated Al Kα X-ray source at 200 W power was used for all scans. All spectra were acquired at a take-off angle of 90° and were charge corrected with respect to the C 1s photoelectric line. Data was processed using CasaXPS software where a Shirley background correction was employed and peaks were fitted to Voigt profiles.

Results and Discussion

Paddle-type electrodes were printed by fused deposition modelling (FDM) using a thermosetting polylactic acid composited with graphitic additives (c-PLA), formed with an 8 wt% graphite weight fraction. The quantity was chosen based on previous investigations that demonstrated the trade-off between intrinsic c-PLA and the brittleness of the resulting solidified printed material.[23,24] High wt% fractions approaching 12% or more resulted in very brittle c-PLA components. More recently, modifying composition so that directly usable 3D printed composites are being developed for use in biosensors for detect SARS-CoV-2.[40] The images and schematic model shown in Fig. 1a shows the typical dimensions of these electrodes. The surface roughness with a periodicity of ~0.8 mm between the filamentary features is characteristic of the FDM printing method and indicative of its resolution using this c-PLA feed material.

PLA electrodes even with conductive additives are ineffective as good electrochemical electrodes as-printed. This is due to the impregnation of the graphitic additives within the PLA. Ensuring sufficient concentration to allow conductivity along any direction of the printed PLA is important (presumably a percolating network of some form along the filament and from the core of the filament to its outer surface), but so too is the relief of the conductive additive on the outer surface.[1,41] For electrodeposition the latter consideration is important to ensure conformal electrodeposition and there are several methods to relive these conductive materials from the PLA matrix. One approach is the use of suitable solvents such as dichloromethane (DCM) and various solvents to improve interfacial electron transfer[42,43] or in situ electrochemical modification[41] during electrochemical polarization or electrolysis.

Other approaches also use a heat treatment to avoid the decomposition issues with solvent decomposition.[44] We use a thermal pre-treatment method that had two distinct benefits: the near-surface graphitic material was exposed as required to create an electrical conductive surface for electrodeposition, and the typically microporous surface of the thermoset PLA was smoothened (Fig. 1d). Using higher weight fractions of graphitic additive (>12 wt% graphite) can improve conductivity overall but results in a brittle thermoset PLA that is fragile. This heat treatment maintains the structure and structural integrity of the PLA print. We heated printed electrodes prior to electrodeposition in ambient air at 300 °C (melting point of PLA is ~220 °C) and in all cases the electrode structure was maintained.

Figures 1b and 1c show the potentiostatic response of these printed c-PLA electrodes in vanadyl sulfate solutions resulting in the electrodeposition of V_2O_5 on the electrode surface. Achieving conformal coating is useful for several reasons, particularly for miniaturised 3D printed batteries, supercapacitors, sensors, electro-catalysts and other technologies where form factor-by-design is possible with 3D printing of useful electrochemical materials and/or electrodes. A deposit of V_2O_5 can be achieved on 3D printed PLA and the potentiostatic curves indicate instantaneous nucleation with non-zero initial current. With a notable absence of a diffusion-limited peak in the current, the charge passes achieves a relatively stable value in time, which is discussed quantitatively further on. Instantaneous nucleation occurs on conductive PLA where the graphitic content at the surface promotes electrodeposition. By comparison, electrodeposition of V_2O_5 in similar electrolytes and under similar conditions onto stainless steel and other metallic substrates results in a current peak, with self-limiting current over extended deposition times.[45] Electrodeposition was carried out on identical electrodes in two separate batches of experiments for two

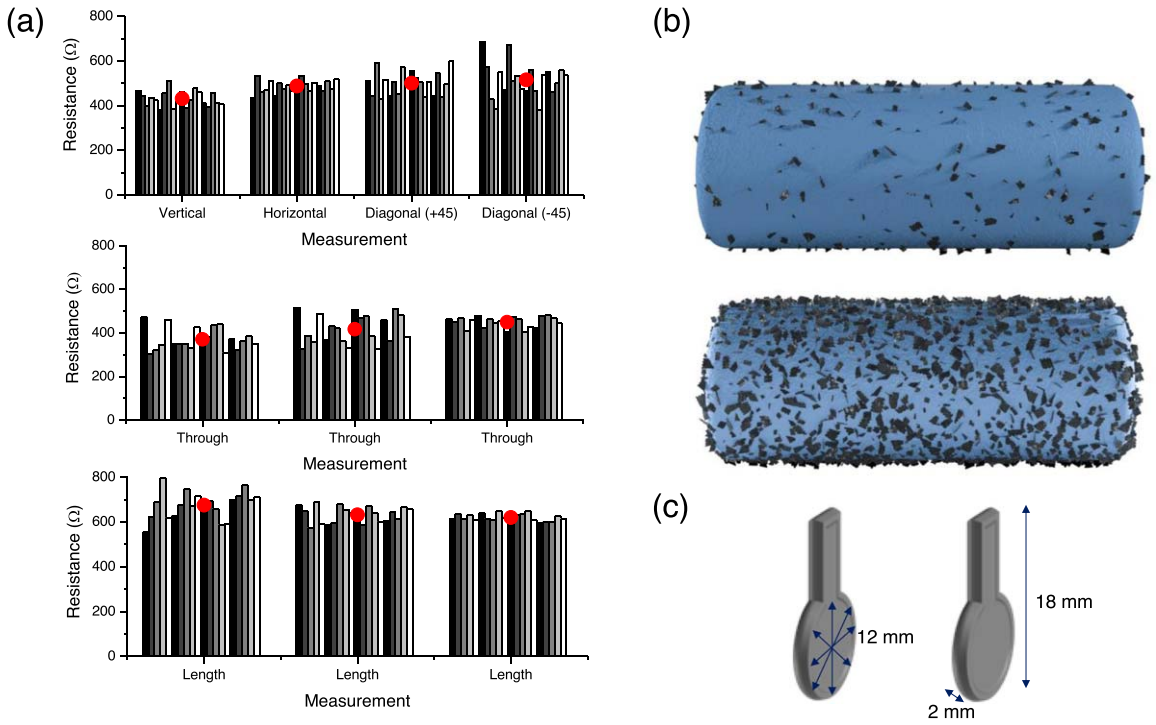

Figure 3. (a) Electrical resistance measurements of the 3D printed c-PLA electrodes along 4 directions from edge to edge of the 12 mm diameter circular electrode region (see (c)), through the 2 mm thickness of the paddle, i.e. a probe touching the front side and the back side of the paddle, and also from top to bottom along its 18 mm length. The mean value is also shown. (b) Schematic representation of the heat-treated PLA filaments showing exposed graphitic features at the surface. This an exaggerated representation, and the graphite is likely exposed within the roughness that develops during heating. (c) The dimensions of the electrodes and directions for electrical measurements shown in (a).

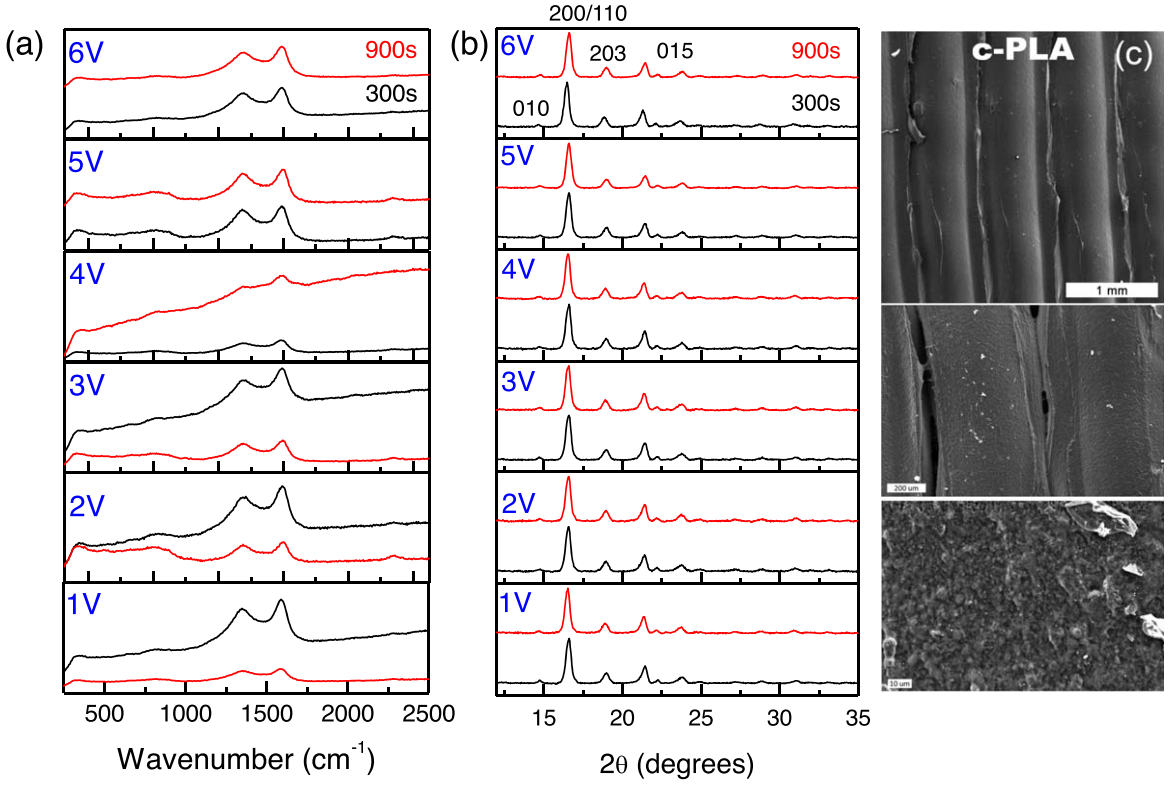

Figure 4. (a) Raman scattering and (b) X-ray diffraction measurements of V_2O_5 films electrodeposited on 3D printed c-PLA electrodes at voltage in the range 1.0–6.0 V over 300s and 900s duration. (c) SEM images of the c-PLA before heat treatment (top) and after heat treatment (middle, bottom). Notable features that occur after heating are some shrinkage/separation between filament in some places, and a roughening of the outer surface wherein the exposed graphitic species reside. The graphite has low contrast as it is conductive in the secondary electron image. The small white features are abraded PLA fragments formed during sample preparation.

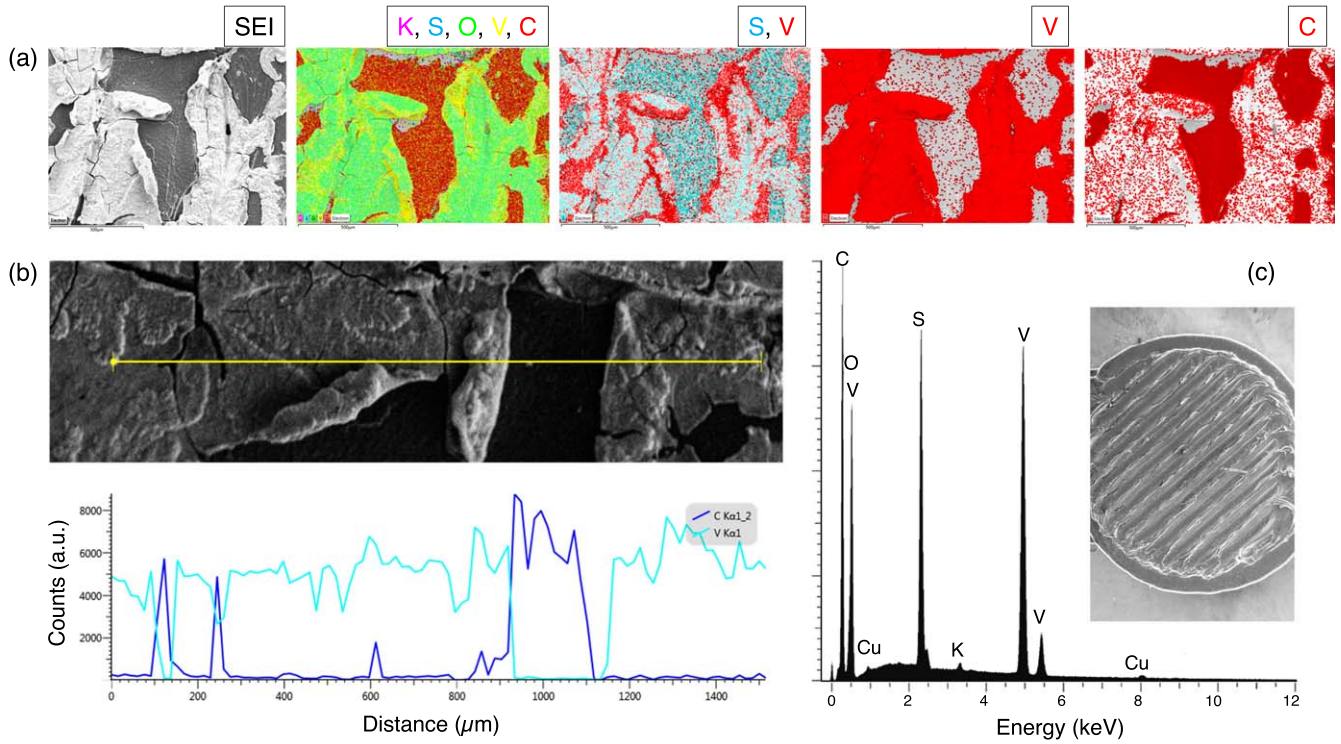

Figure 5. (a) Secondary electron image and various elemental maps of sulfur, carbon, vanadium and oxygen. Each element is color-coded to the legend above it. Potassium as a trace contaminant is also shown. (b) EDX line-scan of a cracked region of V_2O_5 deposit and the underlying c-PLA electrode surface showing the relative at% variation of V and C along the indicated line in the SEM image. (c) Associated EDX spectrum of the fully electrodeposited electrode shown in the inset SEM image.

durations so that we could examine the deposit after 300 s and also after 900 s, especially at voltages where longer durations caused dissolution/delamination of the deposit formed at earlier times.

Without heat treatment, the c-PLA electrode prevents significant electrodeposits from forming on the surface. Figure 1e shows how localized pools of V_2O_5 can be formed in regions between the extruded c-PLA filaments and the surface always remains very sparsely coated. In marked contrast electrodeposition on heat-treated c-PLA electrodes show almost full coverage. The SEM images in Fig. 1f show V_2O_5 film formation across the textured electrode surface and the characteristic cracking is due to the film shrinkage upon drying after removal from the electrolyte. The thickening of the film would be expected to continue while the morphology was porous, allowing continued ionic transport through the film to the electrode surface.

In Fig. 2 the cumulative charge passed as a function of time is shown for V_2O_5 electrodeposition on 3D printed c-PLA electrodes. The cumulative charge varies effectively linearly in time at all potentials for short (Fig. 2a, 300 s) and longer (Fig. 2b, 900 s) deposition durations. The electrodeposition proceeds according to[46]

$$VO^{2+} + H_2O \rightarrow VO_2^{+} + 2H^{+} + e^{-} \quad [1]$$

$$2VO_2^{+} + H_2O \rightarrow V_2O_5 + 2H^{+} \quad [2]$$

In an electrolyte at pH of 0.3–2.2, this is likely the deposition process, although intermediate-based V_2O_5 deposition can occur at pH values above 1.8 up to 3.4.[47] The pH of the electrolyte in this investigation ranged from 1.5–1.8. The theoretical electrodeposited mass was determined using the integrated total charge according to Faraday's law[45,48] leading to V_2O_5 formation. The corresponding coulometric efficiency (Q/m) of the electrodeposition over 300 s and 900 s are shown in Fig. 2c. Electrodeposition over both timeframes confirms a less efficient process at higher voltages. At 2 V, the efficiency is >95%, dropping to just over 3% at 6 V after 900 s deposition. As will be shown, this inefficiency stems from electrolysis in the aqueous electrolyte at voltage >2 V leading to delamination of the film.

We examined many separately printed electrodes that were subject to the heat treatment where the near-surface graphite additive was exposed. A summary of 2-probe electrical measurements is shown in Fig. 3c along each of the 6 directions shown in Fig. 3c. The printing model creates a circular paddle structure where the thermoset filaments are aligned at ∼45° to the long axis.

Transport measurements show that conduction along these filaments, or normal to them does not impact base resistance values after heat treatment. In Fig. 3a, we see that the average resistance is ∼450–500 Ω in 4 directions measured from edge-to-edge of the circular paddle. We ascribe this to a probable melting and connectivity of the filament structures within the composite together with exposure of the surface-bound graphitic conductive additive. Internal resistance of the c-PLA remains consistent irrespective of the direction of measurements. The resistance is slightly less (∼300–400 Ω) when measured through the thickness (2 mm) of the paddle (front side to back side), while the largest resistance as expected (600–700 Ω) is along the full 18 mm length of the electrode when measured from one end to the other. The resistance along the full length scales with distance and consistent with the values measured for the 12 mm paddle disc.

The relatively high resistance observed between opposing sides of the paddle disc of 2 mm thickness is less clear. But based on the extrusion process, we postulate that the graphitic additives are preferentially oriented along the direction of extrusion from the melted filament. Secondly, since the paddle itself is comprised of two layers of thermoset filaments, where the filaments of one layer are located in the inter-filament trough of the second layer and also offset between them. The resistivity along the length of filament with cross-sectional area of ∼0.02 cm^2 is ∼7.2 Ω cm. Nevertheless, at

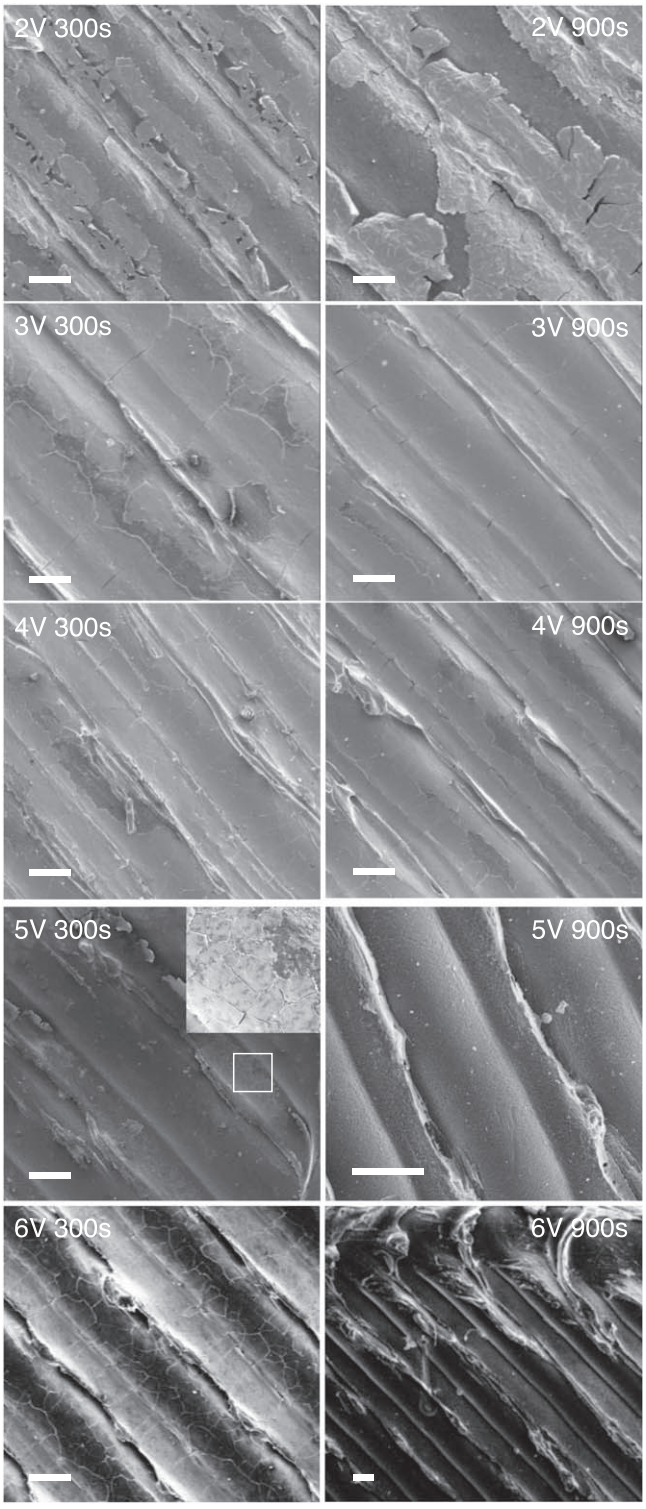

Figure 6. SEM images of the electrodeposited V_2O_5 films on 3D printed c-PLA electrodes after potentiostatic electrodeposition between 2 V and 6 V over 300s and 900s duration in a vanadyl sulfate aqueous electrolyte.

lower voltages, a high degree of coverage of the electrode by electrodeposition is achieved.

After heat treatment, we also examined the c-PLA electrodes coated with electrodeposited V_2O_5 to assess phase purity, crystallinity and composition. Raman scattering and X-ray diffraction characterisation shown in Figs. 4a and 4b respectively confirm the formation of an amorphous phase of V_2O_5 by electrodeposition. In the Raman scattering spectra, the characteristic D (1350 cm^{-1}) band from sp and sp^3 carbons, vacancies, edges sites etc typical of layered graphite, and G-bands (1585 cm^{-1}) related to the presence of in-plane stretching vibration of the sp^2 carbon atoms[49] are easily discerned as they are now exposed on the PLA surface. We do not observe any of the characteristic vibrational modes from the layered orthorhombic V_2O_5 structure, indicating an amorphous phase. Heat treatment that relieves the graphite at the near surface is show in Fig. 4c where graphitic features are exposed over the PLA surface.

The integrity of the printed material is not only maintained, but the post-heated morphology is slightly smoothened and any gaps that sometimes occur between the parallel filaments during printing are a little wider compared to the as-thermoset printed PLA. X-ray diffraction measurements for all voltages and both deposition times also confirm an amorphous V_2O_5 deposit (absence of any reflections from the deposit), and only the reflections from polylactic acid are observed consistent with heat treatment of crystalline PLA.[50] These diffractograms are characteristic of the stable α phase of PLA formed by melt-crystallization after printing and heat treatment.[51,52]

Energy dispersive X-ray analysis of the electrodeposited V_2O_5 on the PLA electrodes was carried out after careful drying. Figure 5a shows a secondary electron image of the V_2O_5 deposit from a region where cracking and peeling occurred so that the deposit and the underlying PLA substrate could be analysed together. The fully coated electrode is shown for reference inset to Fig. 5c. An overlaid elemental map of the SEM image regions for K, S, O, V and C elements is also shown. In separate elemental maps, we show that the V_2O_5 regions and the carbon from the underlying substrate are clearly identified, and also from the EDX line scan across both regions in Fig. 5c. Remnant sulfur species in Figs. 5a and 5d are sometimes found in the small cracks in the V_2O_5 deposited, that were not effectively rinsed out post-deposition.

The nature of the V_2O_5 electrodeposited coating on the 3D printed PLA electrode as was examined using SEM imaging as a function of the deposition time and the applied voltage. Figure 6 below shows a comparison summary of the main features of the electrodeposited films. At 2 V (SCE), we consistently observed patchy coverage of the PLA, but with good coulometric efficiency as shown earlier. Between 2 V and 4 V, the total electrodeposited mass and coverage improve, where the best coatings over the whole textured electrode surface is found at 3 V and 4 V. For electrodeposition at 3 V, the best uniform coverage is found after 900 s. While cracking occurs due to drying, the coverage is relatively uniform across the highly undulating surface of the textured printed PLA. Consistent with an instantaneous nucleation process with non-zero initial current values, film coverage proceeds progressively and for voltage from 2 V–4 V, better coverage is more typical. However, as shown in the comparison between cumulative charge and measured electrodeposited mass discrepancies in Fig. 2, the SEM analysis confirms this where we consistently see very little electrodeposit on the surface at the higher voltages of 5 V and 6 V after 300 s. In Fig. 6, we show the morphology of the electrodeposition in the sparse regions where film growth was observed at 5 V and 6 V after 300 s.

The island structure is evident as observed at lower voltage, but the film is removed after polarization at 5 V and 6 V for 900 s. We postulate that the electrolytic bubbling observed during polarization at these higher voltages leads to delamination of the film over longer durations. Electrodeposition of vanadium (V) oxide at higher voltages/currents is prone to water oxidation. The few regions of V_2O_5 that cover the PLA electrode at these potentials are likely localized oxidizing agents for the aqueous solution, affecting electrolyte pH and continued electrodeposition. This effect is not noticed between 2–4 V for either electrodeposition duration.

While the electrodeposited V_2O_5 films were determined to be amorphous, the stoichiometry and composition from EDX measurements did not provide details on the oxidation state and surface bound species. We used X-ray photoelectron spectroscopy to identify and examine the surface composition of the vanadate film

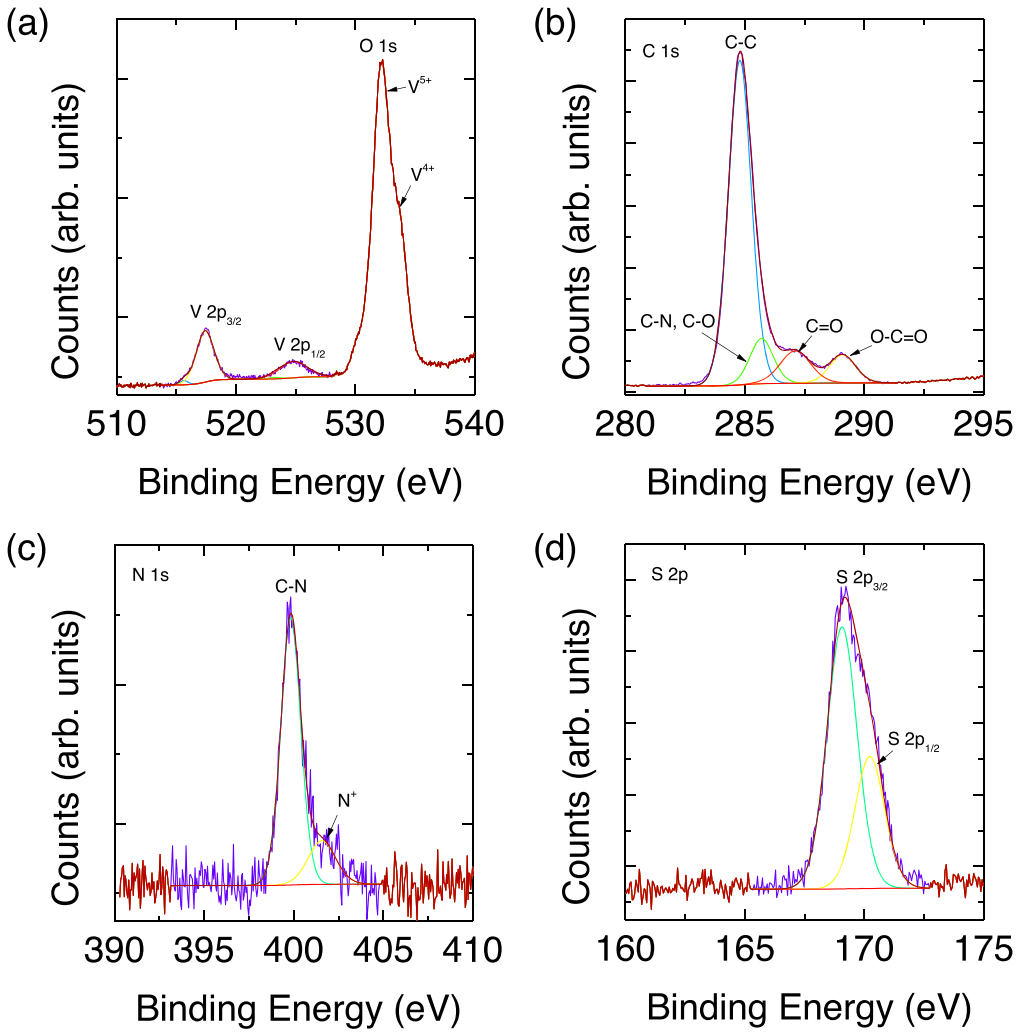

Figure 7. X-ray photoelectron spectra obtained from electrodeposited V_2O_5 on 3D printed c-PLA electrodes. (a) Core-level photoemission from V 2p and O 1s, (b) C 1s, (c) N 1s and (d) S 2p.

on c-PLA. Photoemission spectra of the core level binding energies for V $2p_{3/2}$ and V $2p_{1/2}$ are shown in Fig. 7a. Deconvolution of the V 2p core-levels allows us to determine the vanadium oxidation states. The V $2p_{3/2}$ core-level comprises two photoemission events at ∼517.5 and 515.6 eV from V^{5+} and V^{4+} states respectively.[53] Correspondingly, the high resolution core level spectrum for the O 1s region exhibits two oxygen contributions at ∼533.7 eV from defects and surface species such as hydroxyls, under-coordinated lattice oxygen, or chemisorbed oxygen that is commonly observed for V_2O_5 and several vanadates,[53–55] and at ∼532.2 eV which is usually characteristic of vanadium-oxygen bonds.

The C 1s core-level spectrum in Fig. 7b identifies the bonding within the c-PLA substrate, with C–C, C–O, C–N, C=O and O–C=O groups detected. Traces of nitrogen detected by XPS in Fig. 7c were determined to come from C–N bonds consistent with the C 1s data. The sulfur component detected by EDX was also confirmed by XPS. These sulfur species are likely dried sulfate salts that were found in small cracks in the dried V_2O_5 film that were difficult to completely solubilize and remove. In Fig. 7d, the binding energy of the S 2p core level at ∼169 eV is consistent with sulfate. Overall, the XPS data confirms the V_2O_5 phase formation after electrodeposition.

Conclusions

Coatings of amorphous V_2O_5 can be electrodeposited onto 3D printed thermoset plastics such as polylactic acid (PLA) when the PLA has been impregnated with conductive graphite to improve its electrical conductivity. Thickening of the electrodeposited V_2O_5 is found to be a general response at voltage up to 4 V, and the mass loading controlled by applied voltage. The PLA conductivity is improved by localized melting/dewetting of the PLA to expose the graphite at the surface. Exposed graphitic conductive regions on the outer surface aid in the electrodeposition under potentiostatic conditions. Most of the charge at higher voltages over 15 min electrodeposition does not contribute to V_2O_5 thickening, but is lost to electrolysis or other parasitic reactions. Localized island growth at higher voltages and currents, together with water oxidation aided by the V_2O_5 regions likely contributed to the nearly bare electrode and delamination of V_2O_5 over longer deposition times.

A very high degree of conformal coverage can be obtained on conductive additive-impregnated PLA plastic electrodes under suitable electrodeposition conditions in aqueous solution, which may prove useful for devices or systems that need active electrochemical materials on atypically structured electrodes; 3D printed electrodes from fused deposition modelling have characteristic structure, line widths and minimum dimensions for almost any macroscopic geometry. Heating above the melting point of PLA does not deteriorate the structure when composited with graphite. If intrinsic conductivity can be controlledor improved, plastic electrodes with shapes more complex that planar metals or meshes often used, can inprinciple be coated by electrodeposition.

Acknowledgments

This work was supported by a research grant from Science Foundation Ireland (SFI) under Grant Number 14/IA/2581. This publication has emanated from research conducted with the financial support of Science Foundation Ireland (SFI) and is co-funded under the European Regional Development Fund under the AMBER award, Grant Number 12/RC/2278_2. We thank V. Egorov for providing a software-derived 3D render schematic of the graphite-PLA composite.

ORCID

Colm O'Dwyer https://orcid.org/0000-0001-7429-015X

References

1. V. Egorov, U. Gulzar, Y. Zhang, S. Breen, and C. O'Dwyer, *Adv. Mater.*, **32**, 2000556 (2020).
2. S. A. M. Tofail, E. P. Koumoulos, A. Bandyopadhyay, S. Bose, L. O'Donoghue, and C. Charitidis, *Mater. Today*, **21**, 22 (2018).
3. A. Ambrosi and M. Pumera, *Adv. Funct. Mater.*, **28**, 1700655 (2018).
4. A. Ambrosi and M. Pumera, *Chem. Soc. Rev.*, **45**, 2740 (2016).
5. K. Gnanasekaran, T. Heijmans, S. van Bennekom, H. Woldhuis, S. Wijnia, G. de With, and H. Friedrich, *Applied Materials Today*, **9**, 21 (2017).
6. U. Gulzar, C. Glynn, and C. O'Dwyer, *Curr. Opin. Electrochem.*, **20**, 46 (2020).
7. V. Egorov and C. O'Dwyer, *Curr. Opin. Electrochem.*, **21**, 201 (2020).
8. P. Chang, H. Mei, S. Zhou, K. G. Dassios, and L. Cheng, *J. Mater. Chem. A*, **7**, 4230 (2019).
9. G. X. Gu, C.-T. Chen, D. J. Richmond, and M. J. Buehler, *Materials Horizons*, **5**, 939 (2018).
10. J. Li, M. C. Leu, R. Panat, and J. Park, *Mater. Des.*, **119**, 417 (2017).
11. J. Hu et al., *Adv. Energy Mater.*, **6**, 1600856 (2016).
12. S.-H. Kim, K.-H. Choi, S.-J. Cho, S. Choi, S. Park, and S.-Y. Lee, *Nano Lett.*, **15**, 5168 (2015).
13. M. Wei, F. Zhang, W. Wang, P. Alexandridis, C. Zhou, and G. Wu, *J. Power Sources*, **354**, 134 (2017).
14. J. Ren, Y. Zhang, W. Bai, X. Chen, Z. Zhang, X. Fang, W. Weng, Y. Wang, and H. Peng, *Angew. Chem.*, **126**, 7998 (2014).
15. B. K. Deka, A. Hazarika, J. Kim, Y.-B. Park, and H. W. Park, *Int. J. Energy Res.*, **41**, 1397 (2017).
16. K. Sun, T.-S. Wei, B. Y. Ahn, J. Y. Seo, S. J. Dillon, and J. A. Lewis, *Adv. Mater.*, **25**, 4539 (2013).
17. K. Fu et al., *Adv. Mater.*, **28**, 2587 (2016).
18. C. C. Ho, K. Murata, D. A. Steingart, J. W. Evans, and P. K. Wright, *J. Micromech. Microeng.*, **19**, 094013 (2009).
19. R. R. Kohlmeyer, A. J. Blake, J. O. Hardin, E. A. Carmona, J. Carpena-Núñez, B. Maruyama, J. Daniel Berrigan, H. Huang, and M. F. Durstock, *J. Mater. Chem. A*, **4**, 16856 (2016).
20. F. Zhang, M. Wei, V. V. Viswanathan, B. Swart, Y. Shao, G. Wu, and C. Zhou, *Nano Energy*, **40**, 418 (2017).
21. A. J. Blake, R. R. Kohlmeyer, J. O. Hardin, E. A. Carmona, B. Maruyama, J. D. Berrigan, H. Huang, and M. F. Durstock, *Adv. Energy Mater.*, **7**, 1602920 (2017).
22. E.-H. Kil, K.-H. Choi, H.-J. Ha, S. Xu, J. A. Rogers, M. R. Kim, Y.-G. Lee, K. M. Kim, K. Y. Cho, and S.-Y. Lee, *Adv. Mater.*, **25**, 1395 (2013).
23. C. Reyes, R. Somogyi, S. Niu, M. A. Cruz, F. Yang, M. J. Catenacci, C. P. Rhodes, and B. J. Wiley, *ACS Appl. Energy Mater.*, **1**, 5268 (2018).
24. A. Maurel, M. Courty, B. Fleutot, H. Tortajada, K. Prashantha, M. Armand, S. Grugeon, S. Panier, and L. Dupont, *Chem. Mater.*, **30**, 7484 (2018).
25. C. W. Foster, M. P. Down, Y. Zhang, X. Ji, S. J. Rowley-Neale, G. C. Smith, P. J. Kelly, and C. E. Banks, *Sci. Rep.*, **7**, 42233 (2017).
26. A. Manuel Stephan and K. S. Nahm, *Polymer*, **47**, 5952 (2006).
27. F. Croce, G. B. Appetecchi, L. Persi, and B. Scrosati, *Nature*, **394**, 456 (1998).
28. C.-Y. Lee, A. C. Taylor, A. Nattestad, S. Beirne, and G. G. Wallace, *Joule*, **3**, 1835 (2019).
29. T. S. Wei, B. Y. Ahn, J. Grotto, and J. A. Lewis, *Adv. Mater.*, **30**, 1703027 (2018).
30. H. Ragones, S. Menkin, Y. Kamir, A. Gladkikh, T. Mukra, G. Kosa, and D. Golodnitsky, *Sustainable Energy & Fuels*, **2**, 1542 (2018).
31. E. Cohen, S. Menkin, M. Lifshits, Y. Kamir, A. Gladkich, G. Kosa, and D. Golodnitsky, *Electrochim. Acta*, **265**, 690 (2018).
32. F. Zhang, M. Wei, V. V. Viswanathan, B. Swart, Y. Shao, G. Wu, and C. Zhou, *Nano Energy*, **40**, 418 (2017).
33. X. Liu, R. Jervis, R. C. Maher, I. J. Villar-Garcia, M. Naylor-Marlow, P. R. Shearing, M. Ouyang, L. Cohen, N. P. Brandon, and B. Wu, *Adv. Mater. Technol.*, **1**1600167 (2016).
34. J. Li, V. Mishukova, and M. Östling, *Appl. Phys. Lett.*, **109**, 123901 (2016).
35. D. Vernardou, K. C. Vasilopoulos, and G. Kenanakis, *Appl. Phys. A*, **123**, 623 (2017).
36. J. C. Tan and H. Y. Low, *Additive Manufacturing*, **23**, 294 (2018).
37. G. Gonzalez, A. Chiappone, I. Roppolo, E. Fantino, V. Bertana, F. Perrucci, L. Scaltrito, F. Pirri, and M. Sangermano, *Polymer*, **109**, 246 (2017).
38. J. H. Kim, S. Lee, M. Wajahat, H. Jeong, W. S. Chang, H. J. Jeong, J. R. Yang, J. T. Kim, and S. K. Seol, *ACS Nano*, **10**, 8879 (2016).
39. E. Fantino, A. Chiappone, I. Roppolo, D. Manfredi, R. Bongiovanni, C. F. Pirri, and F. Calignano, *Adv. Mater.*, **28**, 3712 (2016).
40. J. S. Stefano, L. R. Guterres, E. Silva, R. G. Rocha, L. C. Brazaca, E. M. Richter, R. A. Abarza Muñoz, and B. C. Janegitz, *Anal. Chim. Acta*, **1191**, 339372 (2022).
41. D. M. Wirth, M. J. Sheaff, J. V. Waldman, M. P. Symcox, H. D. Whitehead, J. D. Sharp, J. R. Doerfler, A. A. Lamar, and G. LeBlanc, *Anal. Chem.*, **91**, 5553 (2019).
42. M. P. Browne, F. Novotný, Z. Sofer, and M. Pumera, *ACS Appl. Mater. Interfaces*, **10**, 40294 (2018).
43. R. Gusmão, M. P. Browne, Z. Sofer, and M. Pumera, *Electrochem. Commun.*, **102**, 83 (2019).
44. F. Novotný, V. Urbanová, J. Plutnar, and M. Pumera, *ACS Appl. Mater. Interfaces*, **11**, 35371 (2019).
45. E. Armstrong, M. O'Sullivan, J. O'Connell, J. D. Holmes, and C. O'Dwyer, *J. Electrochem. Soc.*, **162**, D605 (2015).
46. D. Rehnlund, M. Valvo, K. Edström, and L. Nyholm, *J. Electrochem. Soc.*, **161**, D515 (2014).
47. E. Potiron, A. Le Gal La Salle, A. Verbaere, Y. Piffard, and D. Guyomard, *Electrochim. Acta*, **45**, 197 (1999).
48. S. O'Hanlon, D. McNulty, and C. O'Dwyer, *J. Electrochem. Soc.*, **164**, D111 (2017).
49. A. Ferrari, J. Robertson, S. Reich, and C. Thomsen, *Philos. Trans. R. Soc. London, Ser. A*, **362**, 2271 (2004).
50. T. Tabi, I. E. Sajo, F. Szabo, A. S. Luyt, and J. G. Kovacs, *Express Polym. Lett.*, **4**, 659 (2010).
51. C. Alemán, B. Lotz, and J. Puiggali, *Macromolecules*, **34**, 4795 (2001).
52. H. Yue, J. P. Fernández-Blázquez, J. J. Vilatela, and E. Pérez, *Polymer Crystallization*, **2**, e10081 (2019).
53. G. Silversmit, D. Depla, H. Poelman, G. B. Marin, and R. De Gryse, *J. Electron. Spectrosc. Relat. Phenom.*, **135**, 167 (2004).
54. D. McNulty, D. N. Buckley, and C. O'Dwyer, *ACS Appl. Energy Mater.*, **2**, 822 (2019).
55. C. Glynn, D. Aureau, G. Collins, S. O'Hanlon, A. Etcheberry, and C. O'Dwyer, *Nanoscale*, **7**, 20227 (2015).